Sensitivity of Hypersonic Dusty Flows to Physical Modeling of the Particle Phase

Eric Ching*
Stanford University, Stanford, California 94305
Michael Barnhardt†
NASA Ames Research Center, Mountain View, California 94035
and
Matthias Ihme‡
Stanford University, Stanford, California 94305

https://doi.org/10.2514/1.A34810

The presence of dust in the Mars atmosphere can adversely affect heat shields of entry vehicles by enhancing erosion and increasing surface heat fluxes. However, the accuracy of numerical simulations investigating these effects is limited due to a lack of well-validated physical models of the particle phase. To address this issue, the sensitivities of computational predictions of dust-induced heating augmentation to different parameters and components of the disperse-phase model are evaluated. In particular, the drag correlation, the Nusselt-number correlation, various contributions to momentum and energy transfer, and particle diameter are examined. Numerical simulations are performed using an Euler–Lagrange methodology, in which the carrier gas is solved with a discontinuous Galerkin method. Very strong sensitivity to the drag correlation, moderate sensitivity to the Nusselt-number correlation, and strong sensitivity to the particle diameter are found. In addition, the quasi-steady drag force and heating rate are the most significant contributors to interphase momentum and energy transfer, respectively. These results can contribute to improving models and identifying knowledge gaps and uncertainties in the appropriate dust conditions.

Nomenclature

C_D	=	drag coefficient
c_d	=	specific heat of particle, J/kg
c_p	=	specific heat at constant pressure, J/kg
c_v	=	specific heat at constant volume, J/kg
D	=	particle diameter, m
d_s	=	distance from stagnation line, m
E	=	total energy per unit mass, J/kg
$\boldsymbol{F}$	=	drag force, N
$\boldsymbol{F}_p$	=	pressure-induced drag, N
$\boldsymbol{F}_{\mathrm{qs}}$	=	quasi-steady drag, N
$\boldsymbol{F}_s$	=	inviscid flux
$\boldsymbol{F}_{\mathrm{thermo}}$	=	thermophoretic force, N
$\boldsymbol{F}_v$	=	viscous flux
Kn	=	Knudsen number
Ma	=	Mach number
m	=	mass, kg
N_b	=	number of basis functions
N_e	=	number of elements
P	=	pressure, Pa
Pr	=	Prandtl number
p	=	polynomial order
Q	=	heating rate, W
Q_{qs}	=	quasi-steady heating, W
Q_{uu}	=	undisturbed–unsteady energy contribution, W
q	=	surface heat flux, $\mathrm{W/m^2}$
Re	=	Reynolds number
R_s	=	sphere radius, m
S	=	molecular speed ratio
$\boldsymbol{S}$	=	source term vector
S_e	=	back-coupled energy transfer, $\mathrm{W/m^3}$
$\boldsymbol{S}_\rho$	=	back-coupled mass transfer, $\mathrm{kg/m^3/s}$
S_ρ	=	back-coupled momentum transfer, Pa/m
T	=	temperature, K
T_{ad}	=	adiabatic wall temperature, K
T_r	=	recovery temperature, K
t	=	time, s
$\boldsymbol{U}$	=	vector of state variables
$\boldsymbol{u}$	=	velocity, m/s
V_d	=	particle volume, $\mathrm{m^3}$
$\boldsymbol{x}$	=	spatial coordinates, m
α	=	accommodation coefficient
β	=	mass loading ratio
γ	=	specific heat ratio
θ	=	polar angle, deg
κ	=	thermal conductivity, W/m/K
μ	=	dynamic viscosity, kg/m/s
ν	=	kinematic viscosity, $\mathrm{m^2/s}$
ρ	=	density, $\mathrm{kg/m^3}$
ϕ	=	test function
Ω	=	computational domain
Ω_e	=	local element

Subscripts

c	=	carrier phase
d	=	disperse phase
e	=	element index
t	=	total quantity
Wall	=	wall quantity
∞	=	freestream quantity

Superscript

e	=	element index

Presented as Paper 2019-0895 at the AIAA SciTech Forum and Exposition, San Diego, CA, January 7–11, 2019; received 17 March 2020; revision received 11 September 2020; accepted for publication 15 October 2020; published online 24 March 2021.

*Ph.D. Student, Department of Mechanical Engineering.
†Research Scientist, Aerothermodynamics Branch; michael.d.barnhardt@nasa.gov.
‡Associate Professor, Department of Mechanical Engineering.

I. Introduction

THE flow environment encountered by spacecraft entering the Martian atmosphere is complex because of the high-enthalpy shock layer and wake that surround the vehicle during its descent. Strong shocks, dissociation and ionization, radiation, thermal nonequilibrium, and other phenomena comprise the physics during atmospheric entry. A unique feature of the Mars atmosphere is the presence of suspended dust particles, which can reach altitudes as high as 60 km during dust storms [1]. These particles, with diameters on the order of micrometers [1], can collide with heat shields at high speeds. A large portion of the kinetic energy of the dust can cause spallation damage via mechanical work [2,3] and increase surface heat transfer via absorption. Additional physical mechanisms can further contribute to dust-induced modification of surface heat fluxes [4]. For example, initially "cold" particles encounter very high temperatures upon entering the shock layer. Smaller particles heat up rapidly and can then transfer the accumulated thermal energy to the cooler boundary layer. Larger particles, on the other hand, only increase in temperature slightly and can cause heat-flux attenuation by extracting thermal energy from the shock layer and boundary layer. Furthermore, as particles decelerate in the shock layer, they transmit momentum and kinetic energy to the gas, which can create an accumulation of energy in the gas that is dissipated into heat. Montois et al. [5] provide a more extensive overview of the interactions among the particles, flow, and vehicle. These dust effects can modify the design of the thermal protection system by, for example, necessitating a thicker heat shield. In this work, the target quantity is dust-induced heating augmentation. We focus on smaller Stokes-number regimes, describing particles that either strike the surface at low speeds or are simply carried by the flow past the body. In this case, the key physics can likely be captured by ignoring particle–particle interactions and only accounting for interphase momentum and energy transfer [6]. Note that this process describes a two-way coupled flow. Four-way coupling (specifically interparticle collisions) would be more important for very high mass loading ratios and larger particles because such particles rebound from the surface at low speeds and mitigate subsequent incident particle impacts [7].

In this study, we employ an Euler–Lagrange formulation developed in the framework of a discontinuous Galerkin (DG) method for solving the carrier phase. Discontinuous Galerkin methods have several advantages over conventional low-order schemes, such as a compact stencil and high-order accuracy on arbitrary meshes. The Euler–Lagrange solver accounts for interphase momentum and energy transfer, and is compatible with curved, high-aspect-ratio elements, specifically in the context of particle search and localization and particle–wall collisions. We previously applied this methodology to simulate hypersonic dusty flow over a sphere and obtained good agreement in the stagnation-point heat flux with experiments conducted by Vasilevskii et al. [8] and Vasilevskii and Osiptsov [9]. However, additional high-quality experimental data over a wide range of conditions are needed for validation before a reliable model for simulating high-speed dusty flows over blunt bodies can be constructed. Therefore, the main objective of this work is to evaluate the influences of different components and parameters of the particle-phase model on the solution. We do this for two different flow environments: a selected flow condition from the set of experiments by Vasilevskii et al. [8] and Vasilevskii and Osiptsov [9], and a specific trajectory point of the ExoMars Schiaparelli lander [10]. We investigate the particle drag coefficient and Nusselt-number correlations, as well as other contributions to particle momentum and energy transfer. We also evaluate sensitivity to particle size distribution, which is another source of uncertainty. The target quantity in this paper is dust-induced heat-flux augmentation (as opposed to erosion) due to large uncertainties associated with erosion modeling. Nevertheless, the findings from this sensitivity study are similarly relevant to dust-induced erosion predictions. This work can help increase awareness of both the importance of different components of the particle model and the major sources of uncertainty in numerical results, as well as support the development of a simple, accurate physical model appropriate for the wide range of flow conditions of interest.

The remaining sections of this paper are ordered as follows: Sec. II describes the governing equations and numerical methods for both the carrier and disperse phases. In Sec. III, we discuss the flow configurations and the aforementioned sensitivities. The final section summarizes the major findings.

II. Mathematical Formulation

This section describes the governing equations for both phases, the DG discretization of the Eulerian phase, and the main features of the particle solver. Further details can be found in Ref. [6].

A. Governing Equations of the Carrier Phase

The governing equations for mass, momentum, and energy of the carrier gas are written in vector form as

$$\partial_t \boldsymbol{U} + \nabla \cdot \boldsymbol{F}_s = \nabla \cdot \boldsymbol{F}_v + \boldsymbol{S} \tag{1}$$

where x denotes the spatial coordinates, t is the time, $\boldsymbol{U}(\boldsymbol{x}, t)$ is the vector of state variables, $\boldsymbol{F}_s(\boldsymbol{U})$ is the inviscid flux, $\boldsymbol{F}_v(\boldsymbol{U}, \nabla\boldsymbol{U})$ is the viscous flux, and $\boldsymbol{S}(\boldsymbol{U}, \nabla\boldsymbol{U})$ is the source term vector that accounts for the back-coupling of the particles to the carrier gas. The terms in Eq. (1) can be expanded as

$$\boldsymbol{U} = \begin{bmatrix} \rho \\ \rho\boldsymbol{u} \\ \rho E \end{bmatrix}, \qquad \boldsymbol{F}_s = \begin{bmatrix} \rho\boldsymbol{u} \\ \rho\boldsymbol{u} \otimes \boldsymbol{u} + P\mathbb{I} \\ \boldsymbol{u}(\rho E + P) \end{bmatrix},$$
$$\boldsymbol{F}_v = \begin{bmatrix} 0 \\ \tau \\ \boldsymbol{u} \cdot \tau - \boldsymbol{q} \end{bmatrix}, \qquad \boldsymbol{S} = \begin{bmatrix} S_\rho \\ \boldsymbol{S}_m \\ S_e \end{bmatrix} \tag{2}$$

where ρ is the fluid density, $\boldsymbol{u}$ is the velocity, P is the pressure, E is the total energy per unit mass, and $\mathbb{I}$ is the identity matrix. S_ρ, $\boldsymbol{S}_m$, and S_e are the back-coupled mass, momentum, and energy transfer, respectively. Pressure can be computed from the ideal gas law. We employ Sutherland's law to compute the dynamic viscosity. The specific heats at constant volume and pressure (c_v and c_p, respectively) are either assumed to be constant, as in Sec. III.A, or calculated from the NASA polynomials [11], as in Sec. III.B. Note that for Mach numbers higher than those considered in this study (approximately 6), chemical reactions and thermal nonequilibrium may need to be taken into account.

B. Discontinuous Galerkin Discretization

The computational domain Ω is partitioned into N_e nonoverlapping discrete elements such that $\Omega = \cup_{e=1}^{N_e} \Omega_e$. The element-local solution $\boldsymbol{U}^e$ is represented as a linear combination of Lagrange polynomial basis functions as

$$\boldsymbol{U}^e(\boldsymbol{x}, t) = \sum_{n=1}^{N_b} \tilde{\boldsymbol{U}}_n^e(t)\phi_n(\boldsymbol{x}) \tag{3}$$

where ϕ_n is the nth Lagrange basis polynomial, and $\tilde{\boldsymbol{U}}^e(t)$ are the polynomial coefficients. N_b, the number of basis functions, is determined by p, the user-prescribed order of the polynomial approximation. Note that the nominal order of accuracy in smooth regions is $p + 1$. The global solution approximation can then be written as

$$\boldsymbol{U} = \oplus_{e=1}^{N_e} \boldsymbol{U}^e \tag{4}$$

Invoking the solution approximation in Eq. (3), multiplying Eq. (1) by ϕ_m, and integrating over the element give

$$\sum_{n=1}^{N_b} d_t \tilde{U}_n^e(t) \int_{\Omega_e} \phi_m \phi_n \, \mathrm{d}\Omega + \int_{\Omega_e} \phi_m \nabla \cdot \boldsymbol{F}_s \, \mathrm{d}\Omega = \int_{\Omega_e} \phi_m \nabla \cdot \boldsymbol{F}_v \, \mathrm{d}\Omega + \int_{\Omega_e} \phi_m \boldsymbol{S} \, \mathrm{d}\Omega \tag{5}$$

The basis coefficients on Ω_e can then be obtained after appropriately performing integration by parts on the flux terms and applying numerical fluxes. In this study, we employ the second form of Bassi and Rebay [12] to define the viscous flux contribution. For the inviscid flux, we employ the original Roe flux function [13] in the case of constant specific heats and the modified Roe solver by Yee et al. [14] in the case of variable specific heats. Gauss–Legendre quadrature with an order of accuracy no less than $2p + 1$ is used to numerically compute integrals. We also employ the shock-capturing scheme described in Ref. [15], in which the shock sensor is based on intra-element pressure variations and smooth artificial viscosity is used for stabilization.

C. Physical Model of the Disperse Phase

The following simplifications are applied to the physical model of the disperse phase to enhance the computational feasibility of simulating a large number of particles. First, each particle is considered to be smooth, spherical, solid, nonrotating, and of fixed size. Second, we assume the particle temperature to be uniform, that is, there is no temperature gradient in the interior of the particle. Interactions among particles, such as particle–particle collisions, are ignored. Only momentum and energy are transferred between the carrier and disperse phases. Finally, we assume the flow to be dilute, such that the volume fraction of the disperse phase can be neglected.

The position, velocity, and temperature (denoted x_d, $\boldsymbol{u}_d$, and T_d, respectively) of a given particle are computed using the following set of ordinary differential equations:

$$\frac{d\boldsymbol{x}_d}{dt} = \boldsymbol{u}_d \tag{6a}$$

$$m_d \frac{d\boldsymbol{u}_d}{dt} = \boldsymbol{F} = \boldsymbol{F}_{\mathrm{qs}} + \boldsymbol{F}_{\mathrm{thermo}} + \boldsymbol{F}_p \tag{6b}$$

$$m_d c_d \frac{dT_d}{dt} = Q = Q_{\mathrm{qs}} + Q_{uu} \tag{6c}$$

where the subscript d denotes the disperse phase; the subscript c denotes the carrier phase; c_d is the specific heat of the particle; and m_d is the particle mass and is computed as $\rho_d(\pi/6)D^3$, where ρ_d is the particle density and D is the particle diameter. $\boldsymbol{F}$ is the overall drag force, and Q is the overall heating rate. The various terms comprising $\boldsymbol{F}$ and Q will be discussed later in this section. Additional contributions to drag and heating not included here are detailed in Refs. [16,17].

1. Drag Coefficient

In compressible disperse, gas–solid flows, the quasi-steady viscous drag is typically the most significant force on the disperse phase, defined as

$$\boldsymbol{F}_{\mathrm{qs}} = \frac{1}{8}\pi D^2 \rho_c (\boldsymbol{u}_c - \boldsymbol{u}_d)|\boldsymbol{u}_c - \boldsymbol{u}_d| C_D \tag{7}$$

where C_D is the drag coefficient. In general, drag-coefficient correlations are functions of the relative particle Reynolds number and the relative particle Mach number, given by

$$Re_d = \frac{\rho_c |\boldsymbol{u}_c - \boldsymbol{u}_d| D}{\mu_c} \tag{8a}$$

$$Ma_d = \frac{|\boldsymbol{u}_c - \boldsymbol{u}_d|}{\gamma R T_c} \tag{8b}$$

where μ is the dynamic viscosity, and γ is the specific heat ratio. In this study, we use four drag-coefficient correlations, specifically those by Boiko et al. [18], Henderson [19], Loth [20], and Melosh and Goldin [21].

The correlation by Boiko et al. [18] is given as

$$C_{D,B} = \left(0.38 + \frac{24}{Re_d} + \frac{4}{Re_d^{0.5}}\right)\left[1 + \exp\left(\frac{-0.43}{Ma_d^{4.67}}\right)\right] \tag{9}$$

This correlation has been successfully employed in interaction of shocks with clouds of particles.

The Henderson drag correlation [19] is suited for the subsonic and supersonic flows in the continuum, transitional, and free-molecular regimes. For $Ma_d < 1$, it is defined as

$$C_{D,H} = \frac{24}{Re_d + S\left(4.33 + \frac{3.65 - 1.53 T_d/T_c}{1 + 0.353 T_d/T_c}\right)\exp\left(-0.247\frac{Re_d}{S}\right)} + \exp\left(-0.5\frac{Ma_d}{Re_d}\right)\left[\frac{4.5 + 0.38(0.03 Re_d + 0.48\sqrt{Re_d})}{1 + 0.03 Re_d + 0.48\sqrt{Re_d}} + 0.1 Ma_d^2 + 0.2 Ma_d^8\right] + 0.6S\left[1 - \exp\left(-\frac{Ma_d}{Re_d}\right)\right] \tag{10}$$

and for $Ma_d > 1.75$

$$C_{D,H} = \frac{0.9 + \frac{0.34}{Ma_d} + 1.86\sqrt{\frac{Ma_d}{Re_d}}\left[2 + \frac{2}{S^2} + \frac{1.058}{S}\sqrt{\frac{T_d}{T_c}} - \frac{1}{S^4}\right]}{1 + 1.86\sqrt{\frac{Ma_d}{Re_d}}} \tag{11}$$

where $S = Ma_d\sqrt{\gamma/2}$ is the molecular speed ratio. For $1 \leq Ma_d \leq 1.75$, linear interpolation is used, giving

$$C_{D,H} = C_{D,H}|_{Ma_d=1} + \frac{4}{3}(Ma_d - 1)(C_{D,H}|_{Ma_d=1.75} - C_{D,H}|_{Ma_d=1}) \tag{12}$$

The Loth drag correlation is similarly applicable to a wide range of flow regimes. It was designed with explicit compressibility and rarefaction effects in mind [20]. For $Re_d > 45$, which represents the compression-dominated regime, it is given as

$$C_{D,L} = \frac{24}{Re_d}\left[1 + 0.15 Re_d^{0.687}\right]H_M + \frac{0.42 C_M}{1 + \frac{42500 G_M}{Re_d^{1.16}}} \tag{13}$$

where C_M, G_M, and H_M are auxiliary functions of Ma_d. For $Re_d < 45$, wherein rarefaction effects become important, the drag coefficient is given by

$$C_{D,L} = \frac{C_{D,Kn,Re}}{1 + Ma_d^4} + \frac{Ma_d^4 C_{D,\mathrm{fm},Re}}{1 + Ma_d^4} \tag{14}$$

where $C_{D,Kn,Re}$ accounts for finite Knudsen-number effects, and $C_{D,\mathrm{fm},Re}$ represents the free-molecular creeping flow limit. The exact forms of C_M, G_M, H_M, $C_{D,Kn,Re}$, and $C_{D,\mathrm{fm},Re}$ can be found in Ref. [20].

The final drag correlation used in this study, by Melosh and Goldin [21], is defined as

$$C_{D,M} = 2 + [C_{D,\mathrm{inc}} - 2]\exp\left(-\frac{3.07\sqrt{\gamma}G}{Re_d}\right) + \frac{H\exp\left(-\frac{Re_d}{2Ma_d}\right)}{\sqrt{\gamma}Ma_d} \tag{15}$$

where $C_{D,\mathrm{inc}} = (24/Re_d)(1 + 0.15 Re_d^{0.687})$ represents the incompressible limit, and the auxiliary functions are given by

$$\log_{10} G = \frac{2.5\left(\frac{Re_d}{312}\right)^{0.6688}}{1+\left(\frac{Re_d}{312}\right)^{0.6688}} \tag{16a}$$

$$H = \frac{4.6}{1+Ma_d} + 1.7\sqrt{\frac{T_d}{T_c}} \tag{16b}$$

This drag correlation represents a more well-defined version of that by Crowe [22], originally created to describe particle motion in a rocket nozzle.

Figure 1 displays the variation of the aforementioned four drag-coefficient correlations with particle Reynolds number at various particle Mach numbers. The gray region denotes the approximate range of interest for the types of flows considered in this study. The Loth [20] and Henderson [19] drag coefficients are relatively similar over all particle Reynolds numbers. The Melosh and Goldin [21] correlation is close to the previous two, except at higher Reynolds numbers. At lower particle Reynolds numbers, the Boiko et al. [18] drag coefficient is significantly greater than the first two correlations.

2. *Nusselt-Number Correlations*

The quasi-steady heating rate represents the convective heat transfer due to the instantaneous difference between the fluid boundary-layer edge and particle surface temperatures. It is expressed as

$$Q_{\mathrm{qs}} = \pi D \kappa_c (T_c - T_d) Nu \tag{17}$$

where κ is the thermal conductivity, and Nu is the Nusselt number. To compute the Nusselt number, we consider the correlations by Fox et al. [23], Carlson and Hoglund [24], and Oppenheim [25]. Designed to take into account compressible and noncontinuum flow effects in the subsonic and supersonic flow regimes, the Fox et al. [23] correlation is given by

$$Nu_F = \frac{2\exp(-Ma_d)}{1+17\frac{Ma_d}{Re_d}} + 0.459 Pr^{0.33} Re_d^{0.55} \frac{1+0.5\exp\left(-17\frac{Ma_d}{Re_d}\right)}{1.5} \tag{18}$$

where Pr is the Prandtl number.

The Carlson and Hoglund [24] correlation, intended for particle motion in rocket exhausts, is defined as

$$Nu_C = \frac{2+0.459 Re_d^{0.55}}{1+3.42\frac{Ma_d}{Re_d}(2+0.459 Re_d^{0.55})} \tag{19}$$

This correlation accounts for high Knudsen and Mach numbers.

Oppenheim developed a Nusselt-number correlation based on a theoretical analysis of convective heat transfer in a free-molecular flow with a Maxwellian velocity distribution [25]. This correlation directly modifies the quasi-steady heating rate as

$$Q_{\mathrm{qs},O} = \pi D^2 \alpha P_c |\boldsymbol{u}_c - \boldsymbol{u}_d| q_O \tag{20}$$

where α is the accommodation coefficient, which expresses the efficiency of energy transfer between a gas and a surface. For simplicity, α is set to unity (also done in Ref. [26]). The nondimensional convective heat flux q_O is calculated as

$$q_O = -\left(2+\frac{j_r}{2}+\frac{j_v}{2}\right)(G_O+F_O)\frac{T_d}{T_c} + \left(S^2+2.5+\frac{j_r}{2}+\frac{j_v}{2}\right)(G_O+F_O) - \frac{G_O}{2} \tag{21}$$

in which j_r and j_v are the number of rotational and vibrational degrees of freedom, respectively, and the auxiliary functions are given by

$$G_O = \frac{\mathrm{erf}(S)}{4S^2} \tag{22a}$$

$$F_O = \frac{1}{4}\left[\frac{\exp(-S^2)}{\sqrt{\pi}S} + \frac{2S^2-1}{2S^2}\mathrm{erf}(S)\right] \tag{22b}$$

This yields a Nusselt number of

$$Nu_O = \frac{Q_{\mathrm{qs},O}}{\pi D \kappa_c (T_{\mathrm{ad}} - T_d)} \tag{23}$$

where T_{ad}, the adiabatic wall temperature, is the value of T_d such that $q_O = 0$ in Eq. (21).

Figure 2 displays the variation of the aforementioned three Nusselt-number correlations with particle Reynolds number at various particle Mach numbers. The gray region denotes the approximate range of interest for the types of flows considered in this study. At lower particle Mach numbers, the Carlson and Hoglund [24] correlation generally gives higher Nusselt numbers. At higher Mach

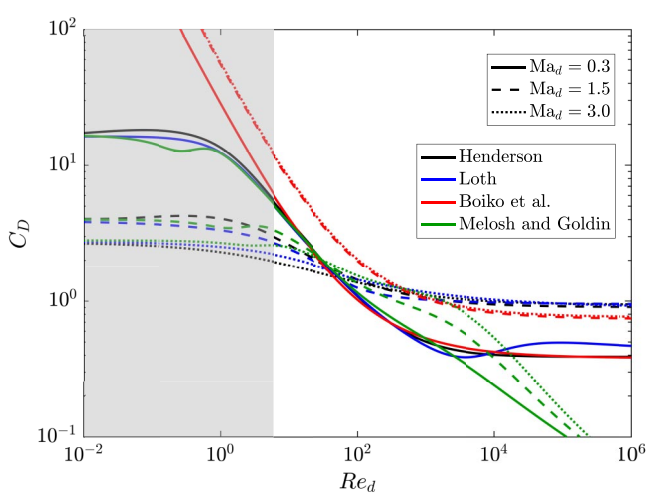

Fig. 1 Variation of different drag-coefficient correlations with respect to particle Reynolds number; three particle Mach numbers are considered: 0.3 (solid lines), 1.5 (dashed lines), and 3.0 (dotted lines).

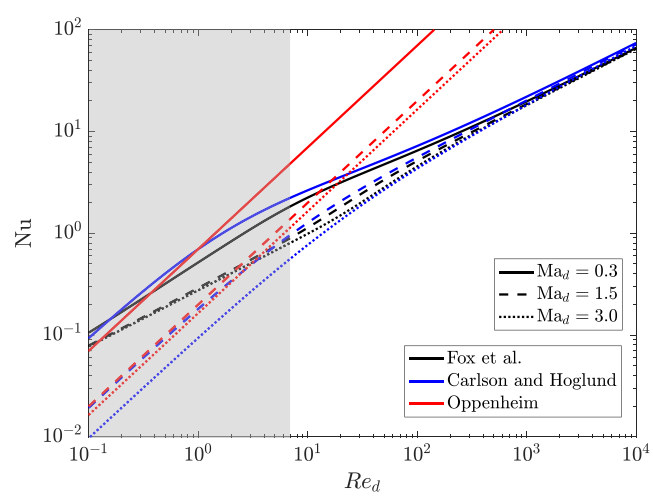

Fig. 2 Variation of different Nusselt-number correlations with respect to particle Reynolds number; three particle Mach numbers are considered: 0.3 (solid lines), 1.5 (dashed lines), and 3.0 (dotted lines).

numbers and lower Reynolds numbers, the Fox et al. [23] correlation yields greater Nusselt numbers. These two correlations converge at high Reynolds numbers (over all Mach numbers). The Oppenheim [25] correlation differs from the other two, especially at higher Reynolds numbers.

3. *Momentum and Energy Contributions*

In compressible flows with solid particles, the quasi-steady drag force and heating rate [Eqs. (7) and (17)] are often the primary contributions to particle momentum and energy transfer, respectively [2,17,26,27]. We aim to investigate whether this is indeed the case in the specific context of high-speed dusty flows over blunt bodies, or if other contributions should be taken into account. As such, we also consider pressure-induced drag, the thermophoretic force, the undisturbed–unsteady contribution to energy transfer, and a modified form of quasi-steady heating.

The first term is given as

$$\boldsymbol{F}_p = -\frac{1}{V_d}\nabla P \tag{24}$$

where $V_d = (\pi/6)D^3$ is the particle volume. This term takes into account the acceleration of a given particle due to the local pressure gradient. It has been included in studies of the interaction of a shock wave with a cloud of particles [18,28].

The second contribution is the thermophoretic force, which arises in regions of high temperature gradients, such as at the shock and in the thermal boundary layer. Collisions between molecules and a given particle are more energetic on the high-temperature side of the particle than on the low-temperature side, causing a net force toward the cooler side [17,20]. To calculate the thermophoretic force, we use the model proposed by Loth [20]. For $Kn_d \leq 0.01$, where $Kn_d = \sqrt{\pi(\gamma/2)}(Ma_d/Re_d)$ is the local particle Knudsen number, the thermophoretic force is computed as

$$\boldsymbol{F}_{\text{thermo}} = -\frac{6\pi\mu_c\nu_c D\left(\frac{2-c_\theta}{c_\theta}\right)(\kappa^* + 2Kn_d c_T)}{\left[1 + 6Kn_d\left(\frac{2-c_\theta}{c_\theta}\right)\right]\left[1 + 2\kappa^* + 4\left(\frac{2-c_\theta}{c_\theta}\right)c_T\right]}\frac{\nabla T_c}{T_c} \tag{25}$$

where $c_\theta = 1.22$ is a tangential momentum coefficient, c_T is a temperature accommodation coefficient, ν is the kinematic viscosity, and $\kappa^* = (\kappa_c/\kappa_d)$ is the thermal conductivity ratio. For $Kn_d \leq 0.01$, it is calculated as

$$\boldsymbol{F}_{\text{thermo}} = -\frac{\pi}{2}\mu_c\nu_c\frac{D}{Kn_d}\frac{\nabla T_c}{T_c}\frac{Kn_d}{1.15 + Kn_d} \tag{26}$$

The undisturbed–unsteady energy contribution is given as [16,17]

$$Q_{uu} = \rho_c c_p \frac{DT_c}{Dt} \tag{27}$$

where (DT_c/Dt) is the substantial derivative of the temperature of the carrier gas. This term accounts for the energy change of the undisturbed ambient thermal field.

Finally, we consider the following modification to the quasi-steady heating rate [Eq. (17)]:

$$Q_{\text{qs},m} = \pi D\kappa_c(T_r - T_d)Nu \tag{28}$$

where T_r is the recovery temperature. This equation is intended to account for the local rise in the temperature of the carrier gas due to dissipative effects near the particle surface. This type of model has been included in several simulations of high-speed particle-laden flows [26,29–31]. In this study, we simply set $T_r = (1 + ((\gamma - 1)/2)Ma_d^2)T_c$ [30,31], which is the local total temperature based on the relative particle Mach number.

D. Particle Solver

In this section, we summarize the algorithmic details of the Lagrangian particle solver. A more complete description can be found in Ref. [6].

A common feature of high-order DG calculations of complex flows is the use of curved elements, instead of more conventional straight-sided elements. Curved elements can significantly improve predictions of particle trajectories due to the increased accuracy of particle–wall collisions [6]. However, tracking particles through curved, high-aspect-ratio elements (which are used in the simulations in this work) is not straightforward. The search–locate algorithm by Allievi and Bermejo [32] is employed to identify the host element of a given particle and map its position in physical to its position in reference space. The state of the carrier gas can be interpolated to the position of the particle using the same polynomial approximation of the element-local Eulerian solution [Eq. (3)]. This approach maintains the order of accuracy of the DG discretization in computing $\boldsymbol{F}$ and Q in Eqs. (6b) and (6c), respectively.

Handling particle–wall collisions is also significantly more challenging on curved, high-aspect-ratio elements than on straight-sided elements. Newton's method is employed to compute the point of collision because, in general, it cannot be obtained analytically. Our developed algorithm efficiently treats hard-sphere collisions by selectively applying the Newton search. It can also deal with a number of pathological cases that can occur only on curved elements.

To reduce computational cost, we represent multiple physical particles as an individual computational particle. The time step of the particle phase is selected such that it is less than or equal to the time step of the carrier phase and the numerical stability of the chosen time stepping scheme is maintained. The effect of the disperse phase is projected to the Eulerian mesh via delta functions, yielding an efficient back-coupling formulation. For the simulations performed in this study, the inclusion of the disperse phase increases computational cost by approximately 70% and memory by about 10%.

III. Numerical Results

This section discusses the sensitivities to the physical model of the disperse phase in two different high-speed dusty flow environments. The first one represents the experimental conditions by Vasilevskii et al. [8] and Vasilevskii and Osiptsov [9], whereas the second one corresponds to a specific location on the trajectory of the Schiaparelli capsule during the recent ExoMars mission [10]. We also establish a baseline disperse-phase physical model, which represents the simplest model that yields accurate predictions of the experimental dusty-gas heat flux.

A. Experimental Conditions by Vasilevskii et al. and Vasilevskii and Osiptsov

In this section, we consider the experiments conducted by Vasilevskii et al. [8] and Vasilevskii and Osiptsov [9] consisting of hypersonic dusty flow over a sphere. They measured the dust-induced heat-flux augmentation at the stagnation point. Note that we partially investigated this configuration in a previous work [6]. Therefore, some details are merely summarized; we refer the reader to Ref. [6] for additional information.

1. *Setup*

Table 1 outlines the flow conditions. The working gas is nitrogen. We assume calorically perfect conditions given the relatively low shock-layer temperatures. In addition, 100,000 second-order hexahedral elements are used to partition the domain, which includes only the sphere forebody. The mesh is refined in the vicinity of the shock to reduce smearing. The cell Reynolds number, defined as

$$Re_{\text{cell}} = \frac{\rho_c a_c h}{\mu_c} \tag{29}$$

Table 1 Flow conditions for hypersonic dusty flow past a sphere based on the experiments by Vasilevskii et al. [8] and Vasilevskii and Osiptsov [9]

Parameter	
Ma_∞	6.1
$P_{t,\infty}$	17.5 bar
$T_{t,\infty}$	570 K
R_s	0.006 m
T_{wall}	300 K
Dust material	SiO_2
ρ_d	2264 kg/m^3
$\overline{D}$	0.19 μm
β	3%

$(\cdot)_\infty$ denotes freestream conditions, $(\cdot)_t$ indicates total quantities, Ma is the Mach number, R_s is the radius of the aluminum sphere, T_{wall} is the wall temperature, ρ_d is the material density of the dust, β is the mass loading ratio, and $\overline{(\cdot)}$ indicates the averaging procedure employed by Vasilevskii et al. [8].

where a is the speed of sound and h is the mesh spacing, is approximately 200 at the shock and 30 at the stagnation point. (Recall the multiple degrees of freedom in each element.) The DG solutions here are computed with $p = 2$ (third-order-accurate) polynomials. No appreciable changes are observed with $p = 3$ (fourth-order-accurate) polynomials. At the inflow boundary, freestream conditions are prescribed for both phases. At the outflow boundary, extrapolation is used for the carrier gas while particles simply exit the domain. Isothermal no-slip conditions are enforced at the sphere wall. Rebound velocities of particles striking the wall are computed using the correlations by Stasenko [33]. We use implicit third-order backward differencing and the third-order Adams–Bashforth method to advance the carrier and disperse phases, respectively. All simulations are run until a quasi-steady state is obtained. Particles are injected along the inflow boundary at random locations. They are assumed to initially be in equilibrium with the freestream gas. Approximately one million computational particles are employed in a given simulation.

The experiments were performed in the UT-1 wind tunnel of the Central Aerohydrodynamic Institute [8,9]. To introduce dust into the flow, a fluidized bed of particles and the pure gas were injected at separate points into the high-pressure chamber upstream of the nozzle and blunt body. Heat fluxes were measured by way of calorimetric sensors. For each flow condition considered, the ratio between the stagnation-point heat flux of the dusty gas (with particles) and that of the pure gas (without particles) was reported.

2. *Baseline Model*

In this section, we establish a baseline physical model of the particle phase. Sensitivities will be investigated with respect to this baseline model, which consists of the Henderson drag coefficient [19], the Nusselt number by Fox et al. [23], and the thermophoretic force [20]. Other contributions to momentum and energy transfer are ignored, yielding $\boldsymbol{F} = \boldsymbol{F}_{\text{qs}} + \boldsymbol{F}_{\text{thermo}}$ and $Q = Q_{\text{qs}}$, which represent the simplest model that accurately predicts the dusty-gas heat flux in the experimental configurations of Vasilevskii et al. [8] and Vasilevskii and Osiptsov [9]. The selection of this model will be further motivated by results discussed later in this section. We emphasize that this model may not necessarily be the most accurate, given experimental uncertainties and the somewhat narrow range of flow conditions investigated thus far. In-depth comparisons with additional experimental data would be required to construct a model that is reliable for all high-speed dusty flow conditions.

Figure 3 displays the dusty-gas temperature field obtained using the baseline model. Sample particle locations, projected onto the xy plane, are included as well. Note that the seemingly low quantity of particles near the stagnation line is due to the sphere-to-plane projection. The shock intersects the stagnation line at $x \approx -.00695$ m. Slight smearing of the shock because of the artificial viscosity is evident; nevertheless, it is adequately captured. There is slight accumulation of particles near the stagnation point due to deceleration in the shock layer and inelastic wall collisions. A small region devoid of particles near the outflow boundary can be observed. This is a result of nonequilibrium between the carrier gas and the particles.

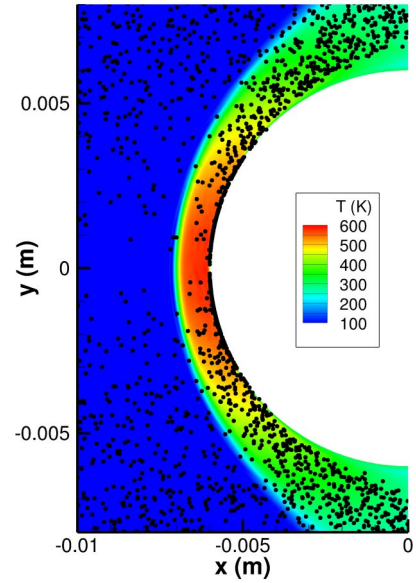

Fig. 3 Dusty-gas temperature field and particle locations for the flow conditions in Table 1; only 0.0001% of the total particles is shown.

Figure 4 shows the dusty-gas heat flux obtained with the baseline model as a function of θ, which is the polar angle with respect to an axis pointing from the sphere center to the stagnation point. The pure-gas heat flux is included as well. There is significant heat-flux augmentation, especially near the stagnation point. The black asterisk represents the experimental dusty-gas heat flux at the stagnation point, computed by scaling the stagnation-point heat-flux ratio from the experiments (reported directly by Vasilevskii et al. [8] and Vasilevskii and Osiptsov [9]) by the pure-gas heat flux from the DG calculations. Good agreement is observed. Additional details on the numerical solution, such as representative particle trajectories, grid convergence studies, and further comparisons between the pure and dusty gases, can be found in Ref. [6].

3. *Particle Trajectory Characteristics*

Before discussing the sensitivity of the heat-flux predictions to the physical model of the disperse phase, we first show the evolution of

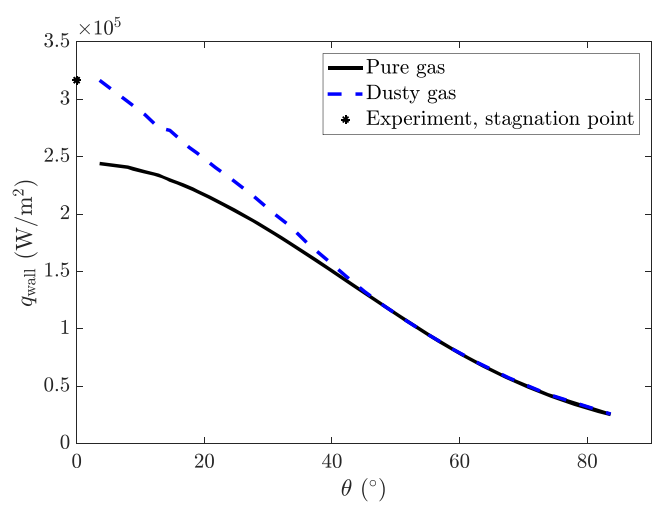

Fig. 4 Pure-gas and dusty-gas surface heat-flux profiles for the flow conditions in Table 1.

various disperse-phase quantities during two representative particle trajectories: the first is initialized at $d_s = 0.1$ mm, where d_s is distance from the stagnation line (normal to the direction of the freestream flow), and the second is initialized at $d_s = 1.8$ mm. Both particles are initialized just ahead of the shock. The following particle quantities are considered: Re_d, Ma_d, C_D, Nu, u_d, and T_d. Figure 5 displays the variation of these quantities as the particles traverse the shock layer until either collision with the sphere surface occurs or the particles leave the domain of interest. As mentioned previously, the particles rebound from the surface according to the coefficients of restitution by Stasenko [33]; however, the reflected trajectory is omitted from Fig. 5 for simplicity. In these figures, $x^* = x/R_s + 1$ is the nondimensionalized streamwise coordinate. The bulk flow moves in the positive x direction. Three different models are considered: the baseline model described above and two variations from the baseline model, namely, the Loth [20] drag correlation (instead of the Henderson [19] correlation) and the Oppenheim [25] Nusselt-number correlation (instead of the Fox et al. [23] correlation). Some smearing of the shock, due to the artificial viscosity stabilization, is evident in these figures from $x^* \approx -0.18$ to $x^* \approx -0.14$. For reference, visualization of the particle trajectories for the baseline model and the Loth [20] correlation is provided in Fig. 6, with $y^* = y/R_s$. The black circles represent the initial particle positions. The shock is located at $x^* \approx -0.14$, the outflow boundary is at $x^* = 1$, and the stagnation point is at $x^* = 0$.

Figures 5a and 5b display the evolution of the relative particle Reynolds and Mach numbers, respectively. For all three models considered, the general trends in these figures are similar. Re_d and Ma_d are initially close to zero due to equilibrium with the freestream. Upon crossing the shock, however, Re_d and Ma_d increase due to the strong nonequilibrium between the two phases given the rapid decrease of the carrier phase velocity. Re_d varies between 0 and 1.4, whereas Ma_d varies between 0 and 1.6. The peaks in the corresponding profiles furthest upstream indicate the locations at

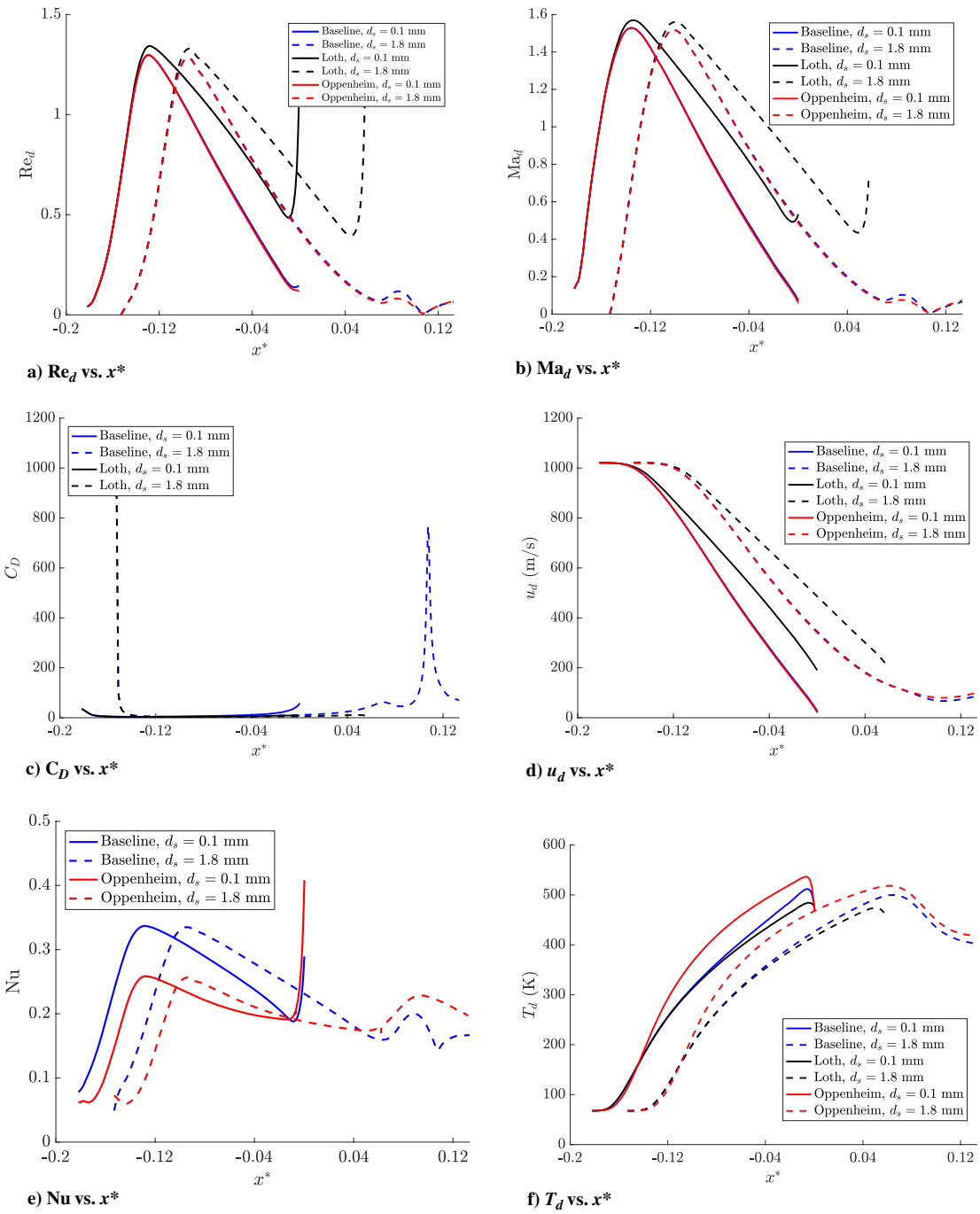

a) Re_d vs. x^*

b) Ma_d vs. x^*

c) C_D vs. x^*

d) u_d vs. x^*

e) Nu vs. x^*

f) T_d vs. x^*

Fig. 5 Evolution of disperse-phase quantities for two particle trajectories: $d_s = 0.1$ mm (solid lines) and $d_s = 1.8$ mm (dashed lines).

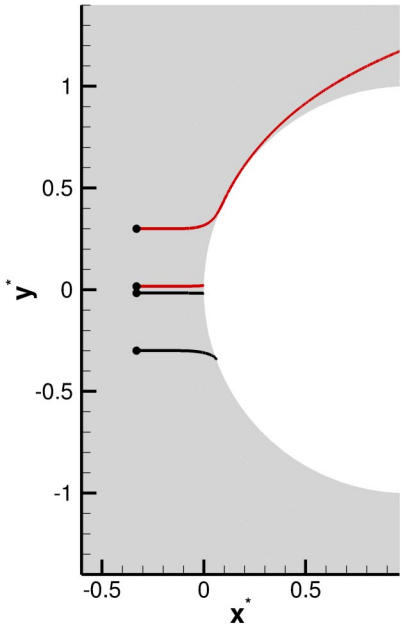

Fig. 6 Particle trajectories for $d_s = 0.1$ mm and $d_s = 1.8$ mm for hypersonic dusty flow over a sphere: baseline model (upper red curves) and Loth [20] drag correlation (lower black curves).

which the particles enter the shock layer. For $d_s = 0.01$ m, all three models predict collision with the surface, as indicated by the abrupt breaks in the corresponding curves in Figs. 5a and 5b. However, only the Loth [20] correlation predicts a sharp rise in Re_d. Furthermore, only the Loth [20] correlation predicts a wall collision for $d_s = 1.8$ mm. This can be explained by examining the values of the drag coefficient and the particle streamwise velocity u_d, which will be discussed next.

Figure 5c shows the values of the drag coefficient for the baseline model and the Loth [20] correlation during the particle trajectories. Near the shock, the Henderson [19] and Loth [20] correlations give very similar values for C_D. However, as the particles traverse the shock layer, the Henderson [19] correlation begins to give greater values for C_D. This causes faster slowdown of the particles and therefore smaller u_d, as shown in Fig. 5d. For $d_s = 1.8$ mm, the sharp spike in the C_D profile occurs because the corresponding particle is advected past the sphere near the wall, where the carrier phase temperature and velocity are small relative to the freestream.

The evolution of Nusselt number during the particle paths is displayed in Fig. 5e for the baseline model and the Oppenheim [25] correlation. Except near the wall, the Fox et al. [23] correlation gives higher values than the Oppenheim [25] correlation. However, inspection of Fig. 5f reveals that the latter predicts higher particle temperatures. This seeming contradiction can be explained by referring to Eq. (23), which shows that in the calculation of the quasi-steady heating rate, the adiabatic wall temperature T_{ad} replaces the typically used carrier phase temperature T_c. In Fig. 5f, for $d_s = 0.1$ mm, the Oppenheim [25] correlation predicts a noticeably sharper decrease in T_d in the boundary layer than the other two models, which indicates faster deposition of thermal energy from the particles to the gas. This increased energy transfer has important implications for the resulting heat-flux profiles, which will be discussed later in this section.

4. *Heat-Flux Sensitivity to Drag Coefficient*

Figure 7 displays the heat-flux profiles computed with the drag-coefficient correlations discussed in Sec. II.C. The Fox et al. [23] Nusselt-number correlation is used for all cases. Given that the drag coefficient directly affects velocity and therefore the particle trajectory, it is unsurprising that there is a significant influence on the heat-flux prediction. Very little heating augmentation is observed with the Boiko et al. [18] correlation, which can be attributed to the substantially greater values of the drag coefficient in Fig. 1. Particles thus

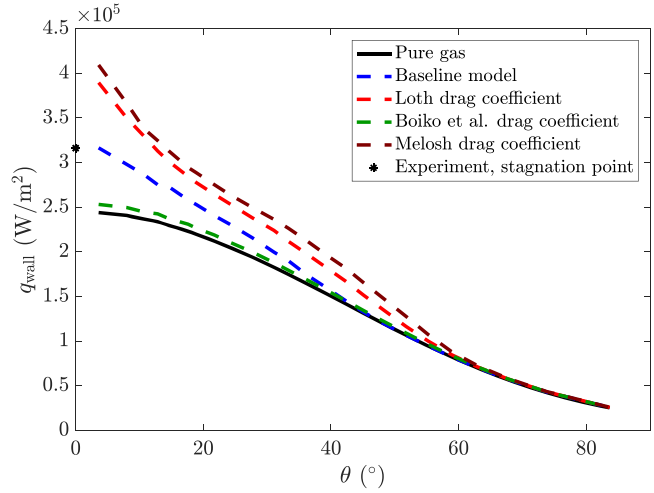

Fig. 7 Dusty-gas heat-flux profiles computed with different drag-coefficient correlations.

decelerate rapidly in the shock layer and are less likely to reach the boundary layer. On the other hand, the Melosh and Goldin [21] and Loth [20] correlations predict much greater heat-flux augmentation than the baseline model because of the higher particle velocities, as shown in Fig. 5d. These particles retain more kinetic energy, which is transferred to the carrier gas near the sphere surface. They also strike the surface at greater speeds, causing the sphere to absorb more energy.

Discrepancies between the Henderson [19] correlation and direct simulation Monte Carlo results have been discussed by Volkov [34], particularly near a Mach number of unity. One possibility, then, to explain why it yields good agreement with experiments is better prediction of drag than the other correlations at Mach and Reynolds numbers less than unity (i.e., when particles approach and enter the boundary layer). Noticeable differences between the Henderson [19] correlation and the other correlations can be observed in Fig. 1 in this regime. At the same time, we note that these results do not necessarily mean that the Henderson [19] drag correlation is better than the other correlations for the given application. Experimental uncertainty and other physical phenomena that are unknown and/or not accounted for here may also play a significant role. We reemphasize that additional test data are required to determine the most appropriate drag correlation or perhaps identify the need for a new correlation.

5. *Heat-Flux Sensitivity to Nusselt Number*

Figure 8 displays the surface heat fluxes computed with the Nusselt-number correlations discussed in Sec. II.C. The Henderson

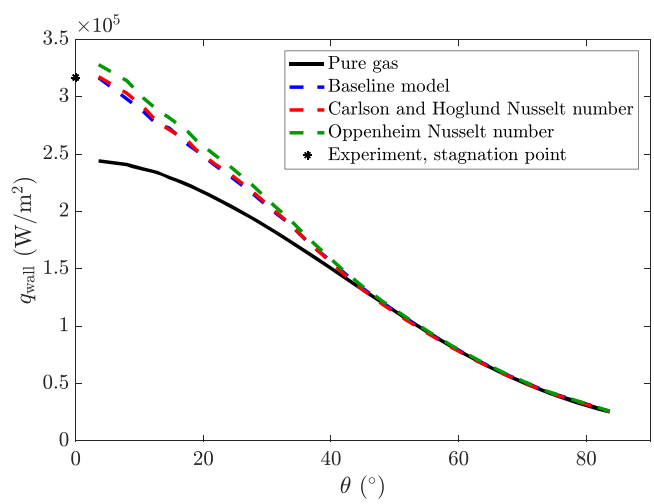

Fig. 8 Dusty-gas heat-flux profiles computed with different Nusselt-number correlations.

[19] drag correlation is used for all cases. Sensitivity to the choice of Nusselt-number correlation is much smaller than to the drag correlation. The Carlson and Hoglund [24] correlation results in approximately the same heat-flux augmentation as the baseline model. The Oppenheim [25] predicts somewhat greater heat-flux augmentation due to the higher particle temperatures and faster energy transfer, as discussed earlier.

6. *Heat-Flux Sensitivity to Momentum and Energy Contributions*

In this section, we investigate the sensitivity of the heat-flux prediction to the momentum and energy contributions discussed in Sec. II.C. Specifically, we examine the effect of adding to the baseline model the following contributions: the pressure-induced drag [Eq. (24)], the undisturbed–unsteady contribution to energy transfer [Eq. (27)], and the quasi-steady heating rate modification [Eq. (28)]. In addition, we examine the effect of excluding the thermophoretic force from the baseline model. Figure 9 displays the resulting dusty-gas heat fluxes. The effects of including the pressure-induced drag force and the undisturbed–unsteady energy contribution are essentially negligible. Excluding the thermophoretic force slightly decreases the predicted heat flux because this force causes acceleration of particles toward the wall in the boundary layer. The modification to the quasi-steady heating rate modestly increases the heat flux due to greater energy transfer between the two phases.

Because of the small but noticeable influence of the thermophoretic force on the results, this term is included in the baseline model. In principle, accounting for the pressure-induced drag force and the undisturbed–unsteady contribution to energy transfer would yield a more accurate model; however, given their negligible influence on the solution, we exclude these terms in favor of a simpler model.

7. *Heat-Flux Sensitivity to Particle Size*

We proceed to examine sensitivity of the heat-flux prediction to particle size, given that there is uncertainty over particle sizes both in experiments and in the context of Mars atmospheric entry. As such, we perform simulations with small variations in the particle sizes. Specifically, we scale the particle diameters by 80 and 120%. The resulting heat fluxes are displayed in Fig. 10. Larger particles yield greater heating, and vice versa for smaller particles, because larger particles collide with the surface at higher speeds. Furthermore, because it takes longer for larger particles to equilibrate with the flowfield, there is increased momentum transfer and work done by drag near the sphere surface.

B. Mars Atmospheric Conditions

We now proceed to investigate more realistic freestream gas conditions observed during Martian entry. Specifically, we target the S5

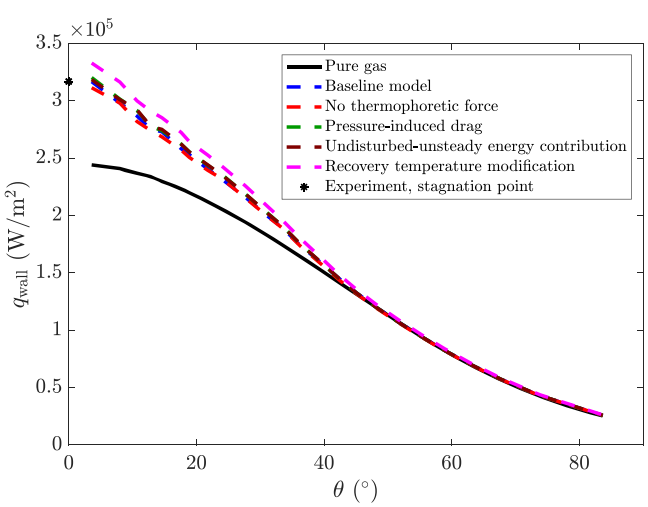

Fig. 9 Dusty-gas heat-flux profiles computed with different modifications to the baseline model, as described in Sec. II.C.

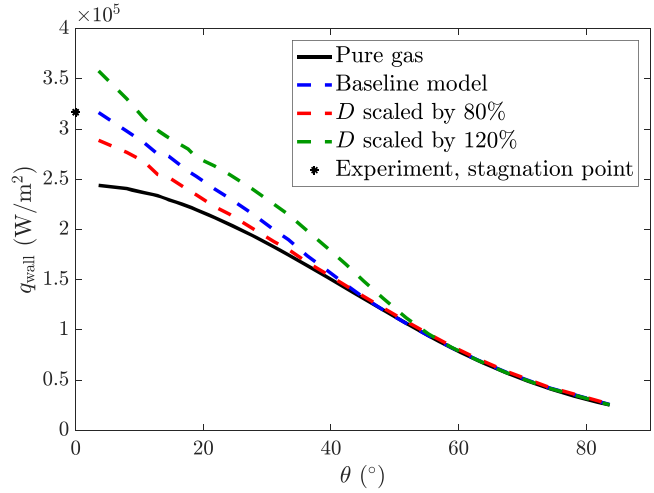

Fig. 10 Dusty-gas heat-flux profiles obtained by considering variations in the particle diameter D: $0.8D$ (red) and $1.2D$ (green); the original particle size distribution is in blue.

trajectory point of the ExoMars Schiaparelli mission [10], summarized in Table 2. For simplicity, we consider a sphere with the same nose radius of 0.6 m as the Schiaparelli capsule. More information on pure-gas (without particles) surface heating of the Schiaparelli capsule can be found in Refs. [35,36]. The stagnation-point heat fluxes in those studies and here are similar; discrepancies can be attributed to slightly different conditions (e.g., freestream values and capsule wall boundary conditions).

The working gas is CO_2. Because of the higher gas temperatures in this configuration, we employ the NASA polynomials to compute specific heats [11] and the Roe solver by Yee et al. [14] that was designed for thermally perfect gases. As done by Ozawa et al. [26] and Majid and Fertig [27], SiO_2 is chosen to represent the dust material. The specific heat of SiO_2 as a function of temperature is obtained from Refs. [37,38]. Although the dust size distribution in the Mars atmosphere is polydisperse [39], we consider monodisperse particles with a fixed diameter of 0.9 μm both to isolate effects of the physical model and to avoid numerical instabilities due to the back-coupling of larger particles. Smooth projection kernels, instead of the delta functions discussed in Sec. II.D, can mitigate this issue and are the subject of an ongoing work [40].

The target quantity for measuring sensitivity to the physical model of the disperse phase is again dust-induced heat-flux augmentation. We reiterate that, although erosion enhancement at times may be of greater interest, we focus here on heat flux because of the complexities of erosion modeling, and our sensitivity results can be similarly applied to predictions of dust-induced erosion. The mass loading ratio β is set to 2.4%, which is likely much larger than typical dust loads in the Mars atmosphere [2,41]. For example, Palmer et al. [3] report $\beta = 0.0069\%$ for a global dust storm and $\beta = 0.00027\%$ during quiescent conditions. Nevertheless, we select a value of β that

Table 2 Flow conditions for simulation of hypersonic flow past a sphere based on the S5 trajectory point of the ExoMars Schiaparelli mission [10]

Parameter	
Ma_∞	5.43
P_∞	114 bar
T_∞	202 K
R_s	0.6 m
Dust material	SiO_2
$\overline{D}$	0.9 μm
β	2.4%

yields notable heat-flux augmentation under the conditions considered to more easily assess sensitivities.

The numerical setup mirrors that in Sec. III.A. We again employ $p = 2$ polynomials and a hexahedral mesh with 100,000 elements of quadratic order. We prescribe the freestream conditions at the inflow, the outflow state is extrapolated from the interior, and the sphere surface is represented by a no-slip isothermal wall that we set to $T = 700$ K. Although this wall temperature is slightly higher than those reported in Ref. [35], the smaller near-wall temperature gradient helps to mitigate numerical instabilities caused by the back-coupling of the particles to the carrier gas. We start with results computed with the baseline model. Figure 11 displays the pure-gas and dusty-gas heat-flux profiles for the baseline model. Similar to the results in Sec. III.A, there is approximately 25% heating augmentation near the stagnation point. However, at $\theta \gtrsim 20$ deg, slight heat-flux reduction is observed, which will be elucidated later in this section.

Figure 12 shows the particle locations computed with the baseline model superimposed on the dusty-gas temperature field. The particle locations are obtained by projecting the global locations onto the xy plane. The seemingly low quantity of particles near the stagnation line is a consequence of the sphere-to-plane projection. Overall, Fig. 12 is qualitatively similar to the corresponding figure for the previous configuration (Fig. 3), but with a higher postshock temperature. The shock, although somewhat smeared due to the artificial viscosity stabilization, is free from apparent oscillations, and it intersects the stagnation line at $x \approx -0.67$ m. Just as in Sec. III.A, there is noticeable accumulation of particles near the sphere surface due to slowdown in the shock layer and inelastic collisions with the surface, as well as a particle-free region near the outflow boundary due to particle inertia.

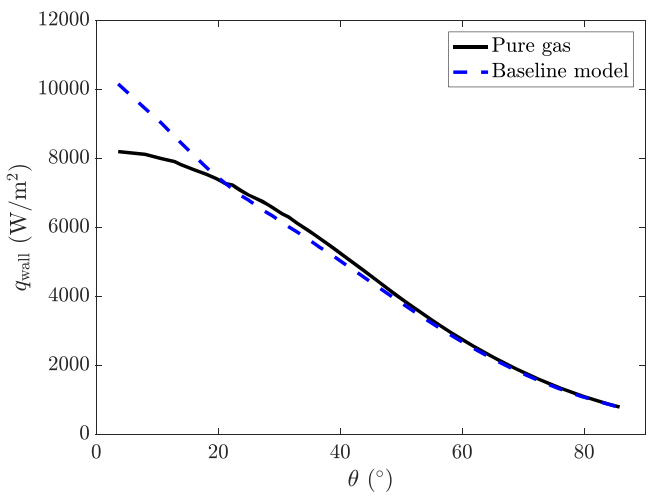

Fig. 11 Pure-gas and dusty-gas surface heat-flux profiles for the flow conditions in Table 2 computed with the baseline model.

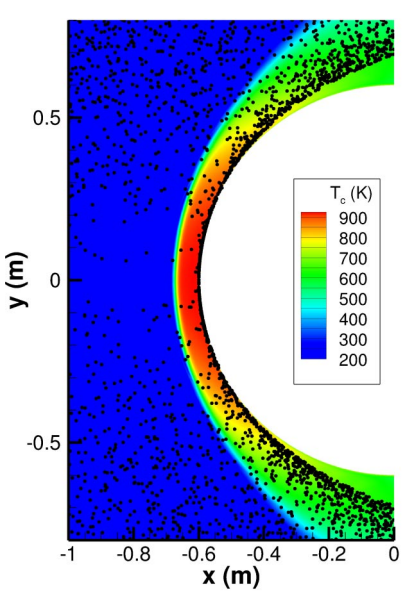

Fig. 12 Dusty-gas temperature field and particle locations for the flow conditions in Table 2; only one millionth percent of the total particles is shown.

Figure 13 shows the variation of the streamwise velocity and temperature of the carrier phase along the stagnation line in the shock layer for the pure-gas and dusty-gas solutions. In these figures, $x^* = x/R_s + 1$ is the nondimensionalized streamwise coordinate, with $R_s = 0.6$ m. The shock is located at $x^* \approx -0.1$, the outflow boundary is at $x^* = 1$, and the stagnation point is at $x^* = 0$. Some smearing of the shock due to the artificial viscosity exists in the upstream region of the u_c and T_c profiles. Initially, u_c is higher in the dusty-gas case because the particles, which retain most of their freestream velocity, transfer momentum to the carrier phase. As the particles traverse the shock layer, they approach the gas velocity, causing the discrepancy in u_c between the two cases to decrease. Nevertheless, u_c for the dusty gas is consistently higher than for the pure gas (until the sphere surface is reached), which contributes to surface heating augmentation by way of increased viscous dissipation near the wall.

We now turn our attention to the T_c profile in Fig. 13b. Initially, T_c is higher in the pure-gas case because particles drain thermal energy from the carrier gas. At $x^* \approx -0.075$, T_c in the dusty-gas solution begins to exceed that in the pure-gas solution. This occurs because particles approach the postshock temperature and due to the work done by drag. Finally, in the boundary layer (indicated by the sharp decrease in T_c in Fig. 13b), the temperature gradient is steeper, which directly results in the amplified heat fluxes displayed in Fig. 11.

1. *Particle Trajectory Characteristics*

Here, we repeat the analysis performed in Sec. III.A of the evolution of various disperse-phase quantities during representative particle trajectories. We again consider the paths of particles initialized just ahead of the shock and at two different distances from the stagnation line (normal to the direction of the freestream flow): $d_s = 0.01$ m and $d_s = 0.18$ m. Particle quantities are plotted in Fig. 14 until the given particle either hits the surface or leaves the domain of interest. We show results for the baseline model (Henderson [19] drag correlation, Fox et al. [23] Nusselt-number correlation, and thermophoretic force) and two variations from the baseline model: the Loth [20] drag correlation (instead of the Henderson [19] correlation) and the Carlson and Hoglund [24] Nusselt-number correlation (instead of the Fox et al. [23] correlation). Slight smearing of the shock caused by the artificial viscosity stabilization is evident in these figures. Figure 15 gives a visualization of the particle trajectories for the baseline model (upper red curves) and the Loth [20] correlation (lower black curves). The black circles represent the initial particle positions.

The relative particle Reynolds and Mach numbers are shown in Figs. 14a and 14b, respectively. The general trends in Figs. 14a and 14b are similar to those for the previous configuration (Figs. 5a and 5b). Re_d and Ma_d are initially close to zero due to equilibrium with the freestream, and then increase when the particles are firmly in the shock layer. The peaks in the corresponding profiles furthest upstream indicate the locations at which the particles enter the shock layer. Re_d varies between 0 and 0.5, whereas Ma_d varies between 0 and 2. For $d_s = 0.01$ m, all three models predict collision with the surface, as indicated by the breaks in the corresponding curves in Figs. 14a and 14b. However, for $d_s = 0.18$ m, only the Loth [20] correlation predicts a particle–wall collision.

The values of the drag coefficient for the baseline model and the Loth [20] correlation during the particle trajectories are displayed in Fig. 14c. The values of C_D are similar between the two models until $x^* \approx -0.06$ and $x^* \approx -0.03$ for $d_s = 0.01$ m and $d_s = 0.18$ m, respectively. The Loth [20] correlation then gives lower C_D than the Henderson [19] correlation, resulting in higher streamwise veloc-

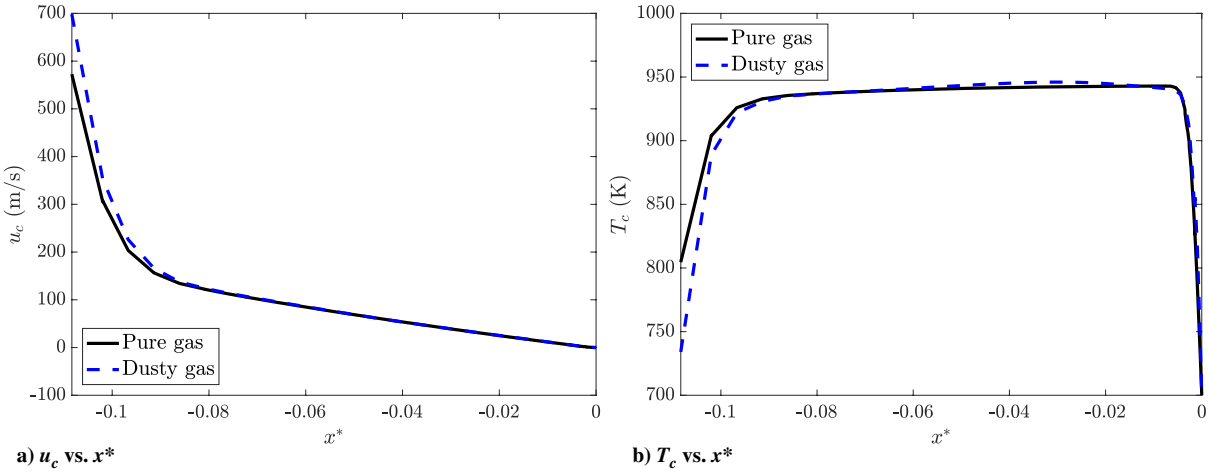

a) u_c vs. x^* b) T_c vs. x^*

Fig. 13 Variation of u_c and T_c along the stagnation line for the pure-gas and dusty-gas solutions.

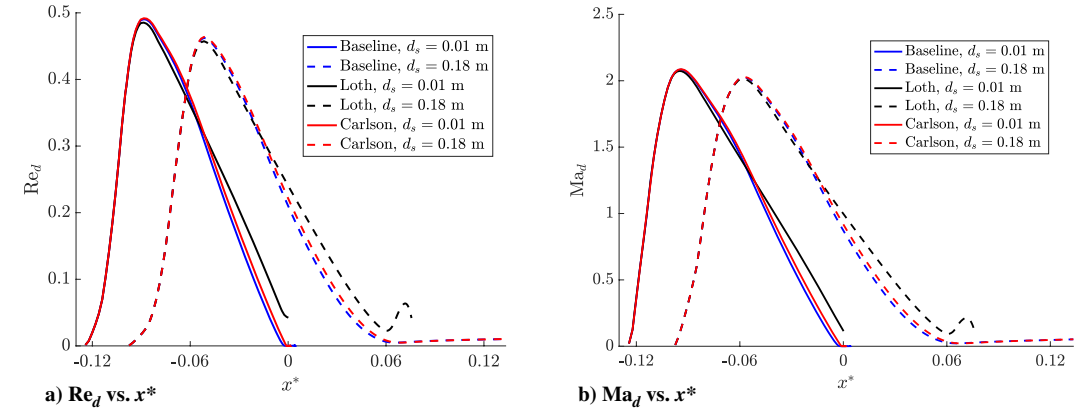

a) Re_d vs. x^* b) Ma_d vs. x^*

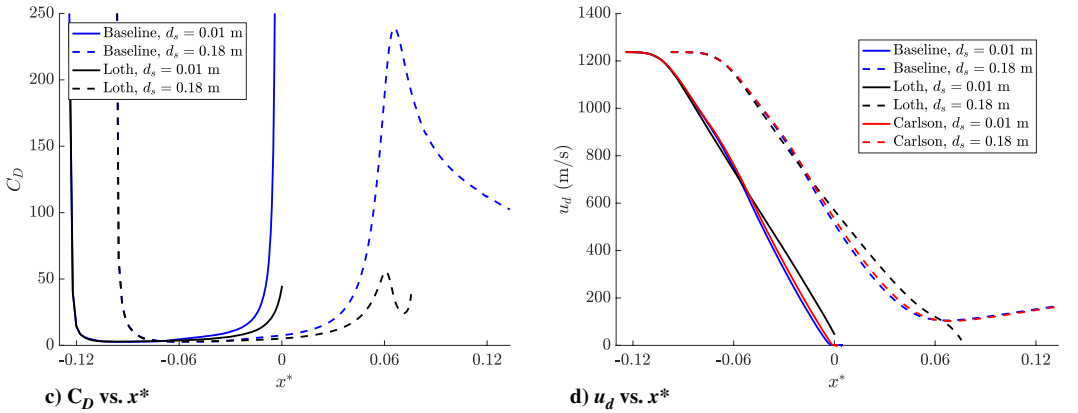

c) C_D vs. x^* d) u_d vs. x^*

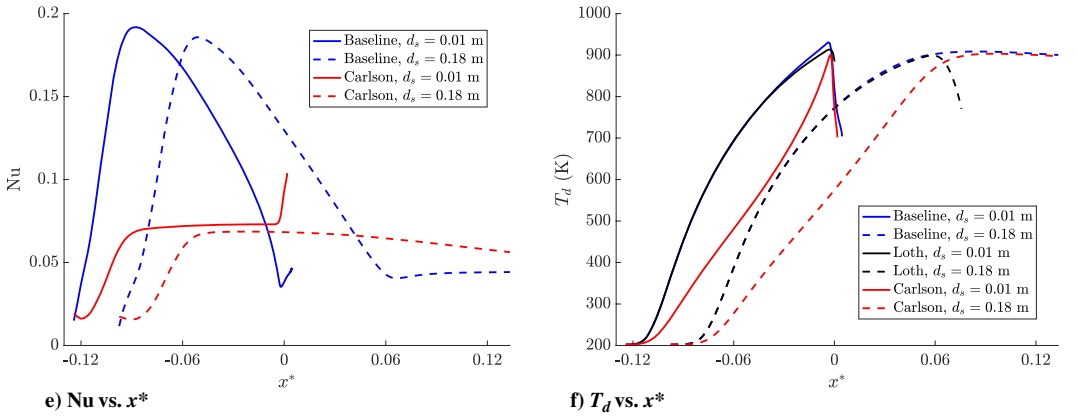

e) Nu vs. x^* f) T_d vs. x^*

Fig. 14 Evolution of disperse-phase quantities for two particle trajectories: $d_s = 0.01$ mm (solid lines) and $d_s = 0.18$ mm (dashed lines).

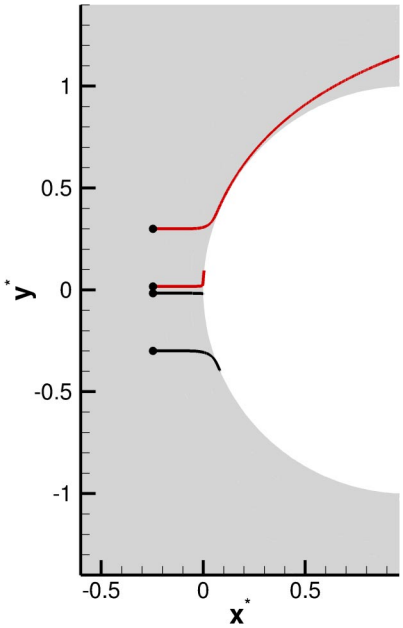

Fig. 15 Particle trajectories for $d_s = 0.01$ m and $d_s = 0.18$ m for hypersonic dusty flow over a sphere: baseline model (upper red curves) and Loth [20] drag correlation (lower black curves).

ities, as illustrated in Fig. 14d. This trend explains why the Loth [20] correlation predicts the particle to hit the sphere surface for $d_s = 0.18$ m, whereas for the other models, the particles are instead advected past the sphere.

Figure 14e shows the values of the Nusselt number for the baseline model and the Carlson and Hoglund [24] correlation during the particle trajectories. The values of Nusselt number differ substantially between the two models even from the beginning of the trajectories. For $d_s = 0.01$ m, the Carlson and Hoglund [24] correlation gives noticeably lower Nusselt numbers than the Fox et al. [23] correlation until $x^* \approx -0.01$. At that point, the former predicts a sharp increase in Nusselt number, whereas the latter yields a rapid decrease in Nusselt number. This difference is reflected in the T_d profiles in Fig. 14f, which illustrate that the Fox et al. [23] correlation predicts a higher maximum particle temperature. However, at $x^* \approx 0$ (very close to the surface), where T_d begins to exceed T_c, the Carlson and Hoglund [24] correlation results in faster energy deposition from the disperse phase to the carrier phase closer to the sphere wall, as indicated by the steeper slope in the T_d curve. A similar trend is observed for $d_s = 0.18$ m, although the particles do not reach the sphere surface (except in the predictions using the Loth [20] correlation).

2. *Heat-Flux Sensitivity to Drag Coefficient*

Figure 16 displays heat-flux profiles computed with the drag-coefficient correlations described in Sec. II.C. The Fox et al. [23] Nusselt-number correlation is used for all cases. Just as in the previous configuration, the Boiko et al. [18] correlation predicts negligible dust-induced heating augmentation. The Loth [20] and Melosh and Goldin [21] correlations predict considerable heat flux augmentation near the stagnation point, which can be explained by referring to Fig. 14 and the earlier analysis. For the $d_s = 0.01$ m trajectories, the Loth correlation predicts particles to reach the sphere surface near the stagnation point at higher velocities and temperatures than does the baseline model. After colliding with the sphere, these particles remain adjacent to the sphere wall at low velocities (not shown in Fig. 14). As a result, the bulk of the thermal energy acquired by the particles from the shock layer is transferred almost directly to the surface. Conversely, since the baseline model yields lower particle velocities, the particles deposit significant thermal energy to the edge of the boundary layer, some of which is advected away from the surface.

For the $d_s = 0.18$ m trajectory, the Loth [20] correlation predicts the particle to reach the sphere surface at $\theta \approx 20$ deg, causing

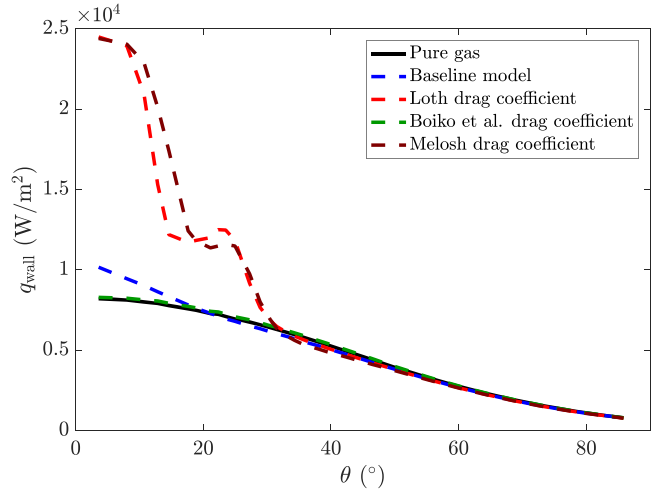

Fig. 16 Dusty-gas heat-flux profiles computed with different drag-coefficient correlations.

momentum and energy transfer from the particle to the carrier gas as well as kinetic energy transfer at the wall. The baseline model, on the other hand, predicts that the particle is simply advected downstream. That particles never reach the wall and only drain thermal energy from the surrounding fluid also explains the slight reduction in heat flux at larger θ. The non-monotonic nature of the heating profiles obtained with the Loth and Melosh correlations is the chance manifestation of the following competing trends as θ increases: the thicker shock layer corresponds to longer residence times and thus lower u_d and higher T_d, while the weaker shock strength corresponds to higher u_d and lower T_d. As in Sec. III.A, these results demonstrate very high sensitivity to the drag correlation. Finally, we note that the observed behavior of the heat-flux profiles computed with the Loth [20] and Melosh and Goldin [21] drag correlations is uncommon. A slight change in the particle diameter yields a more conventional, monotonically decreasing profile (not shown), with less stagnation-point heating augmentation.

3. *Heat-Flux Sensitivity to Nusselt Number*

Heat-flux profiles obtained with the Nusselt-number correlations discussed in Sec. II.C are displayed in Fig. 17. The Henderson [19] drag correlation is used for all cases. The baseline model and the Oppenheim [25] correlation give nearly identical results. Near the stagnation point, the Carlson and Hoglund [24] correlation predicts similar heat-flux augmentation as well. However, at $\theta \gtrsim 20$ deg, the

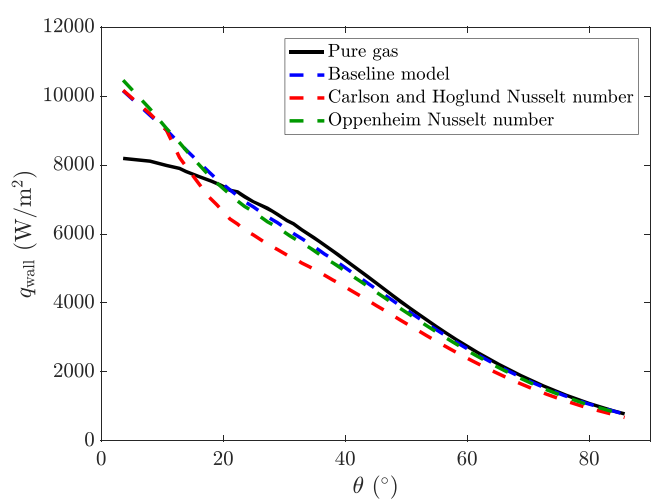

Fig. 17 Dusty-gas heat-flux profiles computed with different Nusselt-number correlations.

Carlson and Hoglund [24] correlation predicts greater dust-induced heat-flux attenuation. This result is explained by examining Fig. 14f, in which the T_d profile corresponding to the Carlson and Hoglund [24] correlation for $d_s = 0.18$ m indicates less energy deposition from the disperse phase to the carrier phase than that for the baseline model. These results illustrate both heat-flux augmentation and attenuation as a result of dust interactions with the flowfield. More so than in the previous configuration (Sec. III.A), the Nusselt-number correlation has a notable influence on the solution, which suggests the importance of the specific flow conditions on the choice of the physical model.

4. *Heat-Flux Sensitivity to Momentum and Energy Contributions*

Figure 18 displays the predicted heat-flux profiles based on the momentum and energy contributions described in Sec. II.C. Again, we investigate the following variations to the baseline model: inclusion of the pressure-induced drag, inclusion of the undisturbed–unsteady contribution to the energy transfer, modification to the quasi-steady heating rate described in Eq. (28), and exclusion of the thermophoretic force. The Henderson [19] drag correlation and Fox et al. [23] Nusselt-number correlation are used for all cases. Similar to what we observe in the previous configuration, the recovery temperature modification yields a moderate increase in the heat flux, and removal of the thermophoretic force results in slight reduction in the heat flux. The pressure-induced drag and undisturbed–unsteady energy contribution have essentially no influence on the heat-flux profiles for these conditions. In general, the conclusion remains the same: the quasi-steady drag and quasi-steady heating rate are the most important terms in the momentum and energy equations for the disperse phase [Eqs. (6b) and (6c), respectively].

5. *Heat-Flux Sensitivity to Particle Size*

In our last set of results, we discuss the influence of particle size on the predicted heat fluxes. Specifically, we consider two additional particle sizes, one slightly smaller and the other slightly larger: $D = 0.8$ μm and $D = 1.0$ μm. Note that in a related study, Ozawa et al. [26] considered particle radii of 1, 2, and 10 μm, and Palmer et al. [3] employed a modified gamma distribution with a mode radius of approximately 0.3 μm.

The heat-flux profiles are displayed in Fig. 19. For $D = 0.8$ μm, the heat flux near the stagnation point is significantly lower. However, for larger θ, there is also less cooling, likely because the particle temperature equilibrates with the gas temperature further upstream than in the $D = 0.9$ μm case. For $D = 1.0$ μm, we again observe substantial stagnation-point heating augmentation and a nonmonotonic heat-flux profile, similar to that obtained for $D = 0.9$ μm with the Loth [20] and Melosh and Goldin [21] correlations (see above). We emphasize that this behavior is rather specific to the conditions

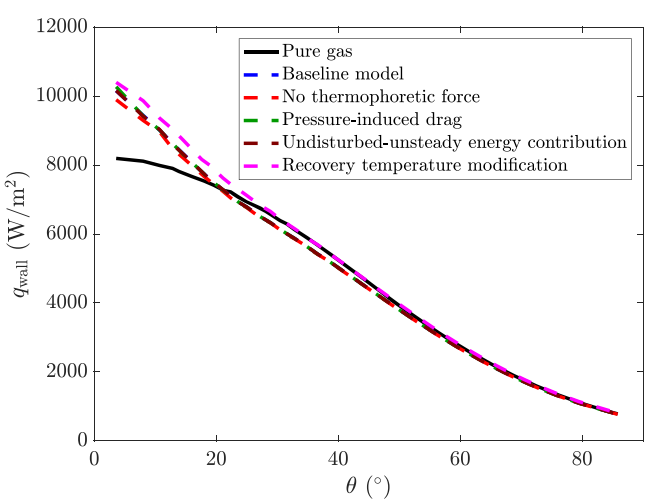

Fig. 18 Dusty-gas heat-flux profiles computed with different modifications to the baseline model, as described in Sec. II.C.

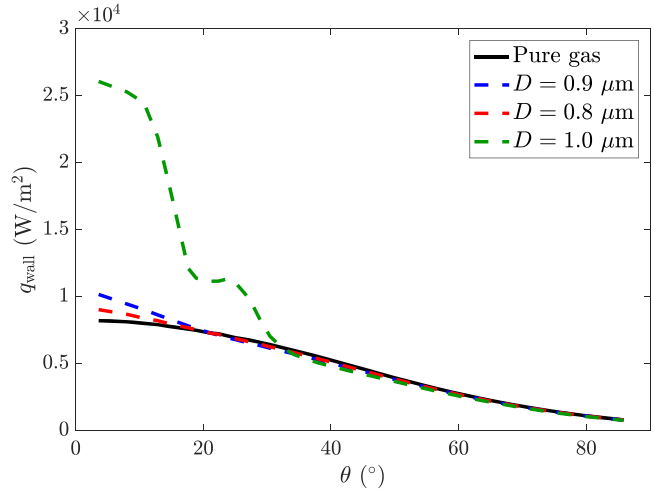

Fig. 19 Dusty-gas heat-flux profiles computed with small variations in the particle diameter $D = 0.8$ μm (red) and $D = 1.0$ μm (green); the original particle diameter, $D = 0.9$ μm, is in blue.

considered. Nevertheless, this illustrates the highly nonlinear interaction between the disperse phase and the carrier phase. For significantly larger particles, collisional energy transfer would dominate over back-coupled momentum and energy transfer, unlike in the simulations presented here. Finally, the primary takeaway is that the results are quite sensitive to the particle size; therefore, it is important to minimize uncertainties in characterizing dust sizes in the Mars atmosphere.

IV. Conclusions

In this work, high-speed dusty flows over spherical blunt bodies are simulated, based on the experiments performed by Vasilevskii et al. [8] and Vasilevskii and Osiptsov [9] and the Mars entry conditions corresponding to a specific point on the trajectory of the ExoMars Schiaparelli mission [10]. A two-way coupled Euler–Lagrange methodology is employed, in which the Eulerian phase is solved using a DG method. The main objective is to examine the influence of the different physical models of the particle phase on predictions of dust-induced heat-flux augmentation. A baseline model that consists of the Henderson drag-coefficient correlation [19], the Fox et al. Nusselt-number correlation [23], and the thermophoretic force [20] is established. This model represents the simplest one that yields good agreement with dusty-gas heat fluxes from experiments. It was found that the heat-flux prediction is very sensitive to the drag-coefficient correlation, whereas the influence of the Nusselt-number correlation is only apparent under the Mars entry conditions. For the flow conditions considered, there is essentially no effect of the pressure-induced drag force and the undisturbed–unsteady energy contribution on the solution. The thermophoretic force has a small yet noticeable influence on the heat-flux prediction. It was also found that the heat-flux prediction is somewhat sensitive to the recovery temperature modification, which has been included in several high-speed particle-laden flow simulations. Finally, the solution is very sensitive to slight changes in particle size. In general, larger particles yield larger heat fluxes and vice versa for smaller particles.

These results illustrate that the quasi-steady drag and heating rate are likely the largest contributors to dust effects on the system. It is critical to use the appropriate drag correlation for the given flow conditions, and the most appropriate correlation can change across different conditions. Desirable test data would include detailed tracking of particle position and temperature as a function of time as particles traverse the shock layer. In particular, these data should lie in the parameter space of $Ma_d < 10$ and $Re_d < 10$, which includes the conditions observed during Mars entry and where differences among common drag correlations are noticeable. It is also important to obtain an accurate particle size distribution, not just for Martian dust, but also for the dust used in experiments because a small error in

the characterization of particle sizes can have noticeable adverse effects on consequent physical modeling. Finally, given the high sensitivities observed in the results and the current lack of relevant experimental results, extensive validation is required to develop a satisfactory physical model that is applicable to a wide range of conditions. Until such an effort is made, it is important to be cognizant of the uncertainties associated with numerical simulations of these types of flows.

Future work will include extending the current DG formulation to greater temperatures so that higher Mach numbers can be analyzed. Erosion enhancement will be also investigated, as well as additional configurations, models, and parameters.

Acknowledgments

This work was supported by a Stanford Graduate Fellowship and an Early Career Faculty grant (NNX15AU58G) from the NASA Space Technology Research Grants Program. Resources supporting this work were provided by the NASA High-End Computing Program through the NASA Advanced Supercomputing Division at NASA Ames Research Center.

References

[1] Papadopoulos, P. E., "Computation of Heat Shield Erosion in a Dusty Martian Atmosphere," Ph.D. Dissertation, Dept. of Aeronautics and Astronautics, Stanford Univ., Stanford, CA, 1994.

[2] Palmer, G., Chen, Y.-K., Papadopoulos, P., and Tauber, M., "Reassessment of Effect of Dust Erosion on Heatshield of Mars Entry Vehicle," *Journal of Spacecraft and Rockets*, Vol. 37, No. 6, 2000, pp. 747–752. https://doi.org/10.2514/2.3646

[3] Palmer, G. E., Ching, E. J., Ihme, M., Kerkhoff, D., and Guelhan, A., "Modeling Heatshield Erosion due to Dust Particle Impacts for Martian Entries," *AIAA SciTech 2020 Forum*, AIAA Paper 2020-0254, Jan. 2020. https://doi.org/10.2514/6.2020-0254

[4] Oesterle, B., Volkov, A. N., and Tsirkunov, Y. M., "Numerical Investigation of Two-Phase Flow Structure and Heat Transfer in a Supersonic Dusty Gas Flow over a Blunt Body," *Progress in Flight Physics*, Vol. 5, June 2013, pp. 441–456. https://doi.org/10.1051/EUCASS/201305441

[5] Montois, I., Pirotais, D., Conte, D., Sauvage, N., and Chazot, O., "Overview of Dust Effects During Mars Atmospheric Entries: Models, Facilities, and Design Tools," *5th International Planetary Probe Workshop*, 2007.

[6] Ching, E. J., Brill, S. R., Barnhardt, M., and Ihme, M., "A Two-Way Coupled Euler-Lagrange Method for Simulating Multiphase Flows with Discontinuous Galerkin Schemes on Arbitrary Curved Elements," *Journal of Computational Physics*, Vol. 405, March 2020, Paper 109096. https://doi.org/10.1016/j.jcp.2019.109096

[7] Volkov, A. N., and Tsirkunov, Y. M., "Effect of a Dispersed Admixture on the Flow Pattern and Heat Transfer in a Supersonic Dusty-Gas Flow Around a Cylinder," *Fluid Dynamics*, Vol. 40, No. 4, 2005, pp. 561–574. https://doi.org/10.1007/s10697-005-0095-3.

[8] Vasilevskii, E. B., Osiptsov, A. N., Chirikhin, A. V., and Yakovleva, L. V., "Heat Exchange on the Front Surface of a Blunt Body in a High-Speed Flow Containing Low-Inertia Particles," *Journal of Engineering Physics and Thermophysics*, Vol. 74, No. 6, 2001, pp. 1399–1411. https://doi.org/10.1023/A:1013996332270

[9] Vasilevskii, E., and Osiptsov, A., "Experimental and Numerical Study of Heat Transfer on a Blunt Body in Dusty Hypersonic Flow," *33rd AIAA Thermophysics Conference*, AIAA 1999-3563, June–July 1999. https://doi.org/10.2514/6.1999-3563

[10] Gülhan, A., Thiele, T., Siebe, F., Kronen, R., and Schleutker, T., "Aerothermal Measurements from the ExoMars Schiaparelli Capsule Entry," *Journal of Spacecraft and Rockets*, Vol. 56, No. 1, 2019, pp. 68–81. https://doi.org/10.2514/1.A34228

[11] McBride, B. J., Zehe, M. J., and Gordon, S., "NASA Glenn Coefficients for Calculating Thermodynamic Properties of Individual Species," NASA TP-2002-211556, 2002.

[12] Bassi, F., and Rebay, S., "GMRES Discontinuous Galerkin Solution of the Compressible Navier-Stokes Equations," *Discontinuous Galerkin Methods: Theory, Computation and Applications*, edited by B. Cockburn, and C. W. Shu, Springer, Berlin, 2000, pp. 197–208. https://doi.org/10.1007/978-3-642-59721-3_14

[13] Roe, P. L., "Approximate Riemann Solvers, Parameter Vectors, and Difference Schemes," *Journal of Computational Physics*, Vol. 43, No. 2, 1981, pp. 357–372. https://doi.org/10.1016/0021-9991(81)90128-5

[14] Yee, H. C., Vinokur, M., and Djomehri, M. J., "Entropy Splitting and Numerical Dissipation," *Journal of Computational Physics*, Vol. 162, No. 1, 2000, pp. 33–81. https://doi.org/10.1006/jcph.2000.6517.

[15] Ching, E. J., Lv, Y., Gnoffo, P., Barnhardt, M., and Ihme, M., "Shock Capturing for Discontinuous Galerkin Methods with Application to Predicting Heat Transfer in Hypersonic Flows," *Journal of Computational Physics*, Vol. 376, Jan. 2019, pp. 54–75. https://doi.org/10.1016/j.jcp.2018.09.016

[16] Ling, Y., Balachandar, S., and Parmar, M., "Inter-Phase Heat Transfer and Energy Coupling in Turbulent Dispersed Multiphase Flows," *Physics of Fluids*, Vol. 28, No. 3, 2016, Paper 033304. https://doi.org/10.1063/1.4942184.

[17] Crowe, C. T., Schwarzkopf, J. D., Sommerfeld, M., and Tsuji, Y., *Multiphase Flows with Droplets and Particles*, CRC Press, Boca Raton, FL, 2011, Chap. 4.

[18] Boiko, V. M., Kiselev, V. P., Kiselev, S. P., Papyrin, A. N., Poplavsky, S. V., and Fomin, V. M., "Shock Wave Interaction with a Cloud of Particles," *Shock Waves*, Vol. 7, No. 5, 1997, pp. 275–285. https://doi.org/10.1007/s001930050082

[19] Henderson, C. B., "Drag Coefficients of Spheres in Continuum and Rarefied Flows," *AIAA Journal*, Vol. 14, No. 6, 1976, pp. 707–708. https://doi.org/10.2514/3.61409

[20] Loth, E., "Compressibility and Rarefaction Effects on Drag of a Spherical Particle," *AIAA Journal*, Vol. 46, No. 9, 2008, pp. 2219–2228. https://doi.org/10.2514/1.28943

[21] Melosh, H. J., and Goldin, T. J., "Heat and Drag Coefficients for Reentry of Impact Ejecta," *39th Lunar and Planetary Science Conference*, Vol. 39, Lunar and Planetary Inst., Houston, TX, 2008, p. 2457.

[22] Crowe, C. T., "Drag Coefficient of Particles in a Rocket Nozzle." *AIAA Journal*, Vol. 5, No. 5, 1967, pp. 1021–1022. https://doi.org/10.2514/3.4119

[23] Fox, T. W., Rackett, C. W., and Nicholls, J. A., "Shock Wave Ignition of Magnesium Powers," *11th International Shock Tubes and Waves Symposium*, Univ. of Washington Press, Seattle, WA, 1978, pp. 262–268.

[24] Carlson, D. J., and Hoglund, R. F., "Particle Drag and Heat Transfer in Rocket Nozzles," *AIAA Journal*, Vol. 2, No. 11, 1964, pp. 1980–1984. https://doi.org/10.2514/3.2714

[25] Oppenheim, A. K., "Generalized Theory of Convective Heat Transfer in a Free-Molecule Flow," *Journal of the Aeronautical Sciences*, Vol. 20, No. 1, 1953, pp. 49–58. https://doi.org/10.2514/8.2523

[26] Ozawa, T., Suzuki, T., Takayanagi, H., and Fujita, K., "Investigation of Martian-Dust Drag and Heat Transfer for Mars Sample Return Mission," *Journal of Thermophysics and Heat Transfer*, Vol. 25, No. 3, 2011, pp. 341–353. https://doi.org/10.2514/1.50714

[27] Majid, A., and Fertig, M., "Two-Phase Flow Solver for Hypersonic Entry Flows in a Dusty Martian Atmosphere," *Journal of Thermophysics and Heat Transfer*, Vol. 30, No. 2, 2016, pp. 418–428. https://doi.org/10.2514/1.T4542

[28] Jacobs, G. B., and Don, W.-S., "A High-Order WENO-Z Finite Difference Based Particle-Source-in-Cell Method for Computation of Particle-Laden Flows with Shocks," *Journal of Computational Physics*, Vol. 228, No. 5, 2009, pp. 1365–1379. https://doi.org/10.1016/j.jcp.2008.10.037

[29] Molleson, G. V., and Stasenko, A. L., "Interaction of a Two-Phase Jet with a Solid Body with Generation of a 'Chaos' of Particles," *High Temperature*, Vol. 51, No. 4, 2013, pp. 537–550. https://doi.org/10.1134/S0018151X13040147

[30] Majid, A., "Two Phase Flow Solver for Solid Particles in Hypersonic Martian Entry Flows," Ph.D. Thesis, Inst. of Space Systems, Univ. of Stuttgart, Stuttgart, Germany, 2012.

[31] Dombrovsky, L. A., Reviznikov, D. L., and Sposobin, A. V., "Radiative Heat Transfer from Supersonic Flow with Suspended Particles to a Blunt Body," *International Journal of Heat and Mass Transfer*, Vol. 93, Feb. 2016, pp. 853–861. https://doi.org/10.1016/j.ijheatmasstransfer.2015.10.072

[32] Allievi, A., and Bermejo, R., "A Generalized Particle Search-Locate Algorithm for Arbitrary Grids," *Journal of Computational Physics*, Vol. 132, No. 2, 1997, pp. 157–166. https://doi.org/10.1006/jcph.1996.5604

[33] Stasenko, A. L., "Velocity Recovery Factors of a Particle Repelled from a Solid Surface," *Journal of Engineering Physics and Thermophysics*, Vol. 80, No. 5, 2007, pp. 885–891. https://doi.org/10.1007/s10891-007-0119-4

[34] Volkov, A. N., "Transitional Flow of a Rarefied Gas over a Spinning Sphere," *Journal of Fluid Mechanics*, Vol. 683, Sept. 2011, pp. 320–345. https://doi.org/10.1017/jfm.2011.267

[35] Pinaud, G., Bertrand, J., Soler, J., Tran, P., and Ritter, H., "Exomars Mission 2016: A Preliminary Post-Flight Performance Analysis of the Heat Shield During Entry on Mars Atmosphere," *AIAA SciTech 2019 Forum*, AIAA Paper 2019-0244, Jan. 2019. https://doi.org/10.2514/6.2019-0244

[36] Brandis, A. M., White, T. R., Saunders, D., Hill, J., and Johnston, C. O., "Simulation of the Schiaparelli Entry and Comparison to Aerothermal Flight Data," *AIAA Aviation 2019 Forum*, AIAA Paper 2019-3260, June 2019.

[37] Touloukian, Y. S., and Buyco, E. H., "Thermophysical Properties of Matter—The TPRC Data Series. Volume 5. Specific Heat—Nonmetallic Solids," Thermophysical Properties Research Center, Purdue Univ. TR ADA951939, Lafayette, IN, 1970.

[38] Chase, M. W., Jr., *NIST-JANAF Thermochemical Tables*, 4th ed., American Inst. of Physics, College Park, MD, 1998, p. 1753.

[39] Tomasko, M. G., Doose, L. R., Lemmon, M., Smith, P. H., and Wegryn, E., "Properties of Dust in the Martian Atmosphere from the Imager on Mars Pathfinder," *Journal of Geophysical Research: Planets*, Vol. 104, No. E4, 1999, pp. 8987–9007. https://doi.org/10.1029/1998JE900016

[40] Ching, E. J., and Ihme, M., "Smooth Projection Kernels for Euler-Lagrange Simulations on Arbitrary Elements Computed with Discontinuous Galerkin Schemes," *AIAA SciTech 2020 Forum*, AIAA Paper 2020-1796, Jan. 2020. https://doi.org/10.2514/6.2020-1796

[41] Papadopoulos, P., Tauber, M. E., and Chang, I.-D., "Heatshield Erosion in a Dusty Martian Atmosphere," *Journal of Spacecraft and Rockets*, Vol. 30, No. 2, 1993, pp. 140–151. https://doi.org/10.2514/3.11522

M. Borg
Associate Editor